

Dehydration studies of natrolites: Role of monovalent extra-framework cations and degree of hydration

YONGMOON LEE¹, DOCHEON AHN², THOMAS VOGT³, AND YONGJAE LEE^{1,4,*}

HPSTAR
400-2017

¹Center for High Pressure Science and Technology Advanced Research, Shanghai 201203, China

²Beamline Research Division, Pohang Accelerator Laboratory, Pohang 37673, South Korea

³Department of Chemistry and Biochemistry & NanoCenter, University of South Carolina, Columbia, South Carolina 29208, U.S.A.

⁴Department of Earth System Sciences, Yonsei University, Seoul 03722, South Korea

ABSTRACT

Rietveld refinements of natrolite analogs [$M_{16}Al_{16}Si_{24}O_{80} \cdot nH_2O$, M-NAT, M = Li, Na, Ag, K, NH₄, Rb, and Cs, 14.0(1) < n < 17.6(9)] at temperatures between 75 and 675 K using synchrotron X-ray powder diffraction reveal the impact H₂O content and monovalent extra-framework cations (EFC) contained in the channels have on dehydration and thermal expansion. Dehydration temperatures are found to be inverse proportional to the size of the EFC. Isostructural K-, Rb-, and Cs-NAT with disordered EFC-H₂O distribution exhibit negative thermal expansions before dehydration. The thermal expansion coefficients increase linearly from K-, Rb-, to Cs-NAT, the latter exhibits has the smallest thermal expansion coefficient of all NAT analogs [$3.0(1) \times 10^{-6} K^{-1}$]. After dehydration, the EFC distribution of K-, Rb-, and Cs-NAT becomes ordered and their thermal expansion coefficients become positive. In the isostructural Li-, Na-, and Ag-NAT with ordered EFC-H₂O distribution, the thermal expansion coefficients are positive for the Li- and Ag-NAT and negative for Na-NAT. After dehydration, this behavior is reversed, and Li- and Ag-NAT show negative thermal expansion coefficients, whereas Na-NAT exhibits a positive thermal expansion. Upon dehydration, the channels in Li- and Ag-NAT reorient: the rotation angles of the fibrous chain units, ψ , change from 26.4(2)° to -29.6(2)° in Li-NAT and from 22.3(2)° to -23.4(2)° in Ag-NAT. The structure models of the dehydrated Li- and Ag-NAT reveal that the change in the channel orientation is due to the migration of the Li⁺ and Ag⁺ cations from the middle of the channel to the walls where they are then coordinated by four framework oxygen atoms. Further heating of these dehydrated phases results in structural collapse and amorphization. X-ray O1s *K*-edge absorption spectroscopy reveals that the binding energy between the EFC and the oxygen of the framework (O_f) is larger in Li- and Ag-NAT than in Cs-NAT due to an increase of the basicity of the framework oxygen. The interaction between the H₂O molecules and EFCs allow a clear separation in structures with disordered H₂O molecules in the center of the channels (K-, NH₄-, Rb-, and Cs-NAT) and those in close proximity to the aluminosilicate framework (Li-, Na-, and Ag-NAT), which leads to systematic dehydration and thermal expansion behaviors. Our structure work indicates that the effects of EFCs are more important to stabilize the NAT structure than the degree of hydration.

Keywords: Thermal expansion, natrolite, dehydration, rietveld refinement, oxygen *K*-edge X-ray absorption spectroscopy

INTRODUCTION

Natrolite (Na-NAT, Na₁₆Al₁₆Si₂₄O₈₀ · 16H₂O) is one of the first zeolites reported in the literature in the early 1800s (Klaproth 1803). Temperature-driven structural changes have been studied as early as 1890 by Rinne (1890), and dehydrated phases have been reported by Baur and Joswig (1996), Fang (1963), Reeuwijk (1972), and Wang and Bish (2008). Understanding the influence extra-framework cations (EFC) have on the dehydration of natrolite phases has been only recently possible after a synthesis route was found to substitute the original sodium cations by alkali (Li⁺, Rb⁺, Cs⁺), alkaline earth (Ca²⁺, Sr²⁺, Ba²⁺), and selected heavy-metal (Cd²⁺, Pb²⁺, Ag⁺) cations. This was achieved at good yields by using the disordered phase of K-exchanged natrolite (Lee et

al. 2013, 2010, 2011b) as a starting reactant.

There are two families of NAT analogs with distinct arrangements of the EFC and H₂O molecules in their pores: in Li-, Na-, and Ag-NAT the EFC are located near the middle of the pores and the H₂O are found closer to the aluminosilicate framework, while in K-, NH₄-, Rb-, Cs-NAT the H₂O molecules are disordered and found near the middle of the pores while the EFC are located in closer proximity to the aluminosilicate framework. DFT calculations (Kremleva et al. 2013) have shown that the H₂O-framework interactions are stronger in the Li- and Na-NAT and different behaviors of these two families are also found at high pressures in the presence of water (Seoung et al. 2013) and non-pore-penetrating pressure-transmitting fluids (Hwang et al. 2015).

In earlier work, we reported on the temperature-dependent structural changes of larger alkali metal substituted NAT, i.e.,

* E-mail: yongjaelee@yonsei.ac.kr

K-, NH₄-, Rb-, and Cs-NAT with disordered cation-H₂O arrangements in their pores (Lee et al. 2011a, 2011c). We found that the dehydration temperatures and the extent to which the framework collapses depend inversely on the size of the extra-framework cation. Here we compare the thermal behavior of the two NAT families as it relates to the location and bonding of the H₂O molecules and EFC in the pores.

EXPERIMENTAL METHODS

The preparation of Li-, Ag-, and Cs-NAT was described in detail by Lee et al. (2010, 2011b). The characteristics of Li-, Ag-, Cs-NAT at high temperatures between 25 and 1100 K were measured by thermogravimetric analysis (TA instruments, TGA2050) at the Korea Basic Science Institute—Seoul Center. A heating rate of 10 K/min under nitrogen atmosphere was used. In situ high-temperature synchrotron X-ray powder diffraction experiments were performed at the X14A beamline at the National Synchrotron Light Source (NSLS-I) at Brookhaven National Laboratory (BNL). The primary white beam from the bending magnet was directed toward a Si(111) crystal selecting monochromatic X-rays with a wavelength of 0.7297(1) Å. Powdered samples were packed into 1.0 mm quartz capillaries, which were connected to a vacuum to facilitate dehydration. The capillaries were then placed inside a heating coil (Stahl and Hanson 1994). From RT to 725 K, the temperature was increased by 25 or 50 K increments under a low vacuum. A heating rate of ca. 25 K/min was used, and the temperature was then stabilized for about 10 min before measurement. A Si-strip detector consisting of a monolithic array of 640 silicon diodes connected to a set of BNL HERMES integrated circuits (D.P. Siddons, private communication) was used to collect high-resolution powder diffraction data ($\Delta d/d \sim 10^{-3}$). The Si-strip detector covered 3.2° in 2θ and was stepped in 2° intervals over the angular range of 3–30° with counting times of 10 s per step. The wavelength of the incident beam was determined using a LaB₆ standard (SRM 660a).

In situ low-temperature experiments were performed at the 9B beamline at the Pohang Light Source (PLS) at Pohang Accelerator Laboratory (PAL). The incident X-rays were vertically collimated by a mirror and using a double-crystal Si (111) monochromator to select a wavelength of 1.4639(1) Å. The detector arm of the vertical scan diffractometer is composed of six sets of Soller slits, flat Ge (111) crystal analyzers, anti-scatter baffles, and scintillation detectors, each set separated by 20°. Specimens of ca. 0.2 g powder were measured as flat plates. The samples were sealed using a beryllium cap and cooled from RT to ca. 75 K in 50 K decrements under a low vacuum. A cooling rate of ca. 25 K/min was used, and the temperature was then stabilized for about 10 min before measurement. Step scans were performed from 10° in 2θ with 0.005° increments allowing for 2° overlaps to the detector banks up to 131° in 2θ . The wavelength of the incident beam was determined using a LaB₆ standard (SRM 660b).

The structural models of the hydrated Li- and Ag-NAT (Li-NAT-hyd and Ag-NAT-hyd, respectively) and their dehydrated forms at 625 K (Li-NAT-deh, Ag-NAT-deh) were obtained using Rietveld refinement (Larson and von Dreele 1986; Rietveld 1969; Toby 2001). For comparison, structural models of Cs-NAT-hyd and Cs-NAT-deh were used from our previous study (Lee et al. 2010, 2011c). Temperature-dependent changes in the unit-cell lengths and volume were derived from a series of whole profile fitting procedures using the GSAS suite of programs (Toby 2001). The background was fitted using a Chebyshev polynomial with $\times 20$ coefficients, and the pseudo-Voigt profile function of Thompson et al. (1987) was used to model the observed Bragg peak shape. The March-Dollase function (Dollase 1986) was used to account for preferred orientation. To reduce the number of parameters, isotropic displacement factors were refined by grouping the framework tetrahedral atoms, the framework oxygen atoms, and the non-framework cations, respectively. Geometrical restraints on the T-O (T = Si, Al) and O-O bond distances of the tetrahedra were applied: the distances between Si-O and Al-O were restrained to target values of 1.620 ± 0.001 and 1.750 ± 0.001 Å, respectively, and the O-O distances to 2.646 ± 0.005 Å for the Si-tetrahedra and 2.858 ± 0.005 Å for the Al-tetrahedra. Difference Fourier syntheses confirmed that the channels in the dehydrated materials do not contain significant electron densities from residual H₂O molecules. In the final stage of the refinements, the weights of the restraints on the framework were maintained. Convergence was

achieved by refining simultaneously all background and profile parameters, scale factor, lattice constants, 2θ zero, preferred orientation function, and the atomic positional and thermal displacement parameters. The final refined parameters are summarized in Supplemental¹ Table 1, and selected bond distances and angles are listed in Supplemental¹ Table 2.

To understand the local structural changes near the EFCs and H₂O molecules, X-ray absorption spectroscopy (XAS) measurements were performed at beamline BL 10-1 at the Stanford Synchrotron Radiation Lightsource (SSRL). Oxygen K-edge spectra that result from O 1s \rightarrow 2p dipole transitions were measured. A bulk-sensitive fluorescence yield (FY) method was employed using linearly polarized X-ray photons at ultrahigh-vacuum (UHV) conditions near ca. 1×10^{-9} Torr. Dehydration at ambient temperatures due to UHV appears to be negligible as the spectrum of hydrated Cs-NAT shows a clear difference from that of dehydrated Cs-NAT.

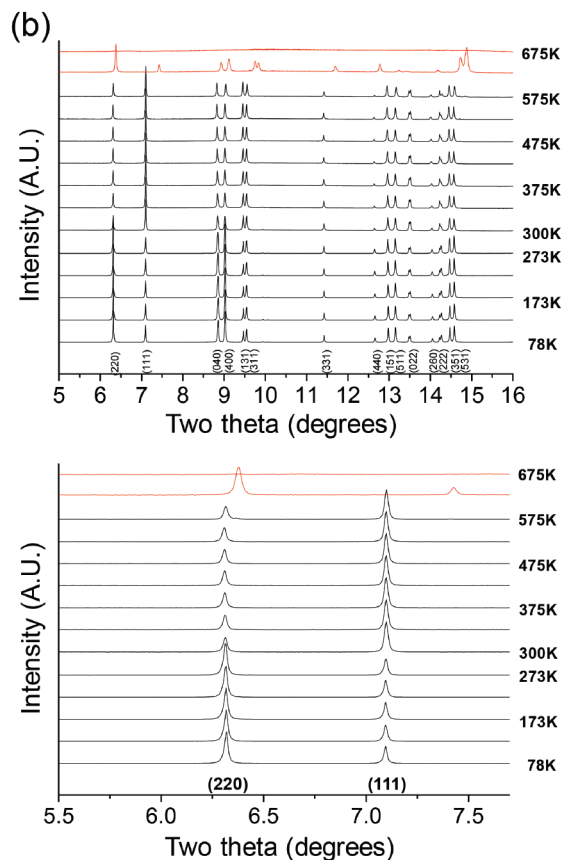
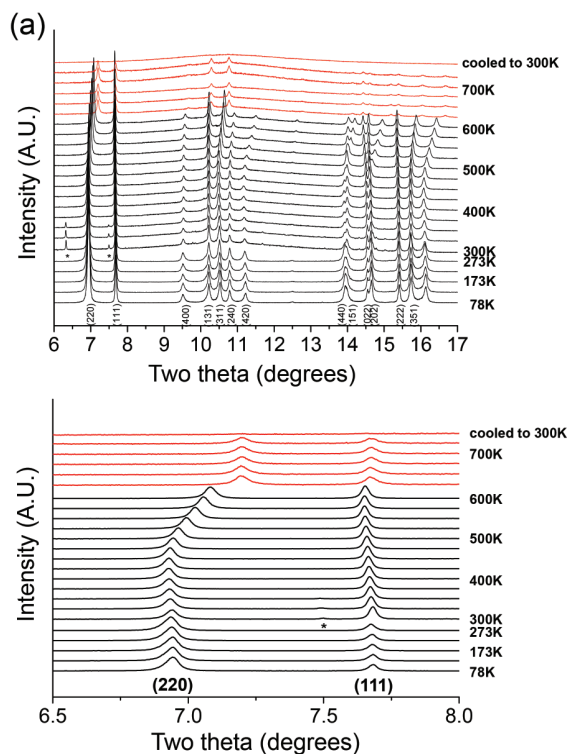
RESULTS AND DISCUSSION

Synchrotron X-ray powder diffraction patterns of Li-, Ag-, and Cs-NAT are shown in Figure 1. At room temperature (RT), all diffraction peaks can be indexed and their crystallographic models agree with previous studies (Lee et al. 2010, 2011b). Dehydration temperatures T_d of Li-, Ag-, and Cs-NAT are 625(25), 575(50), and 375(25) K, respectively. Combined with those of Na-[550(20) K] (Baur and Joswig 1996), K-[450(25) K], and Rb-NAT[425(25) K] (Lee et al. 2011c) one observes that T_d varies inverse with the size of EFCs (Fig. 2a).

Ambient and dehydrated structural models were obtained by Rietveld refinement, and the orientations of the elliptical channels in the *a-b* plane are depicted in Figure 3. At ambient conditions the EFC in Li- and Ag-NAT are located near the middle of the channel surrounded by H₂O molecules (Figs. 3a and 3c, respectively). In the case of Cs-NAT, two disordered Cs⁺ cations are distributed in proximity to the walls along the major axis and ordered H₂O molecules are located near the middle of the channel. The EFCs in Li- and Ag-NAT are sixfold-coordinated, i.e., fourfold-coordinated to framework oxygen and twofold-coordinated to the oxygen atom of the H₂O molecules. In contrast, each Cs⁺ cation in the Cs-NAT is eightfold-coordinated: the coordination number of Cs⁺ with framework O atoms is 6 in the dehydrated and 7 in the hydrated. This tight “stuffed” interatomic arrangement in the Cs-NAT channels hinders the rotation of the NAT chains. As a result, this rigid framework material has the lowest thermal expansion of all NAT analogs.

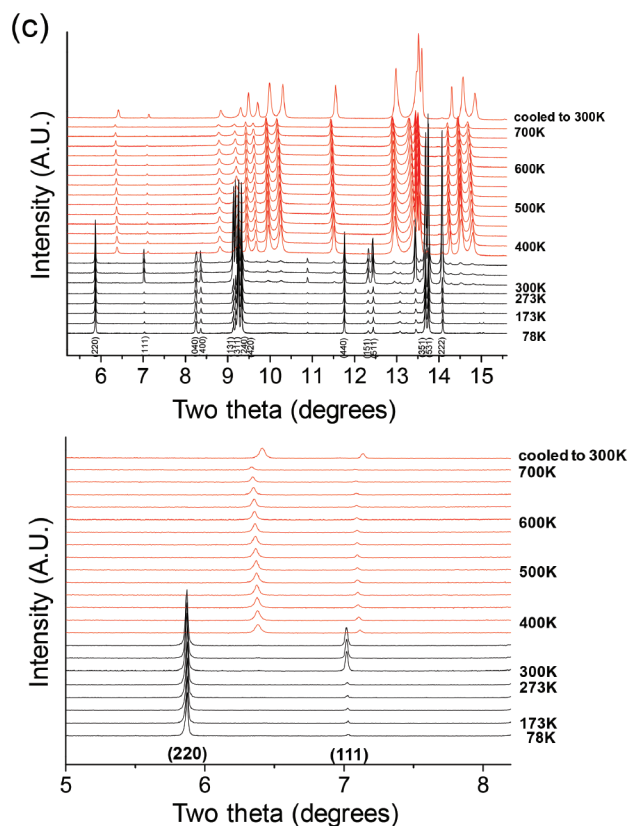
A fibrous chain rotation angle, ψ , defines the geometry of the helical 8-ring channel in the projected *a-b* plane (Pauling 1930). The chain rotation angle ψ is quantitatively measured as an average angle between the quadrilateral sides of the secondary building unit, T₃O₁₀. Large ψ describe a more elliptical channel (see Fig. 3). The chain rotation angle of both Li-NAT and Ag-NAT are 26.4(2)° and 22.3(2)°, respectively. The channel of Li-NAT is more elliptical than the one of Ag-NAT. After dehydration, Li⁺ and Ag⁺ migrate from near the middle of the channel to its side (Figs. 3a and 3c). Furthermore, the channel orientations described by the location of the minor and major axis are inverted [Li-NAT: 26.4(2)° to -29.6(2)° and Ag-NAT: 22.3(2)° to -23.4(2)°]. The EFC move ca. 2.0(1) Å in the case of Li-NAT and ca. 3.4(1) Å in Ag-NAT during dehydration. These large displacements of Li⁺ and Ag⁺ during dehydration are the main reason for the inversion of the elliptical channels in this type of NAT structure. The coordination of the EFC is different before and after dehydration: initially each EFC is sixfold-coordinated to

¹Deposit item AM-17-75902, CIF and Supplemental Material. Deposit items are free to all readers and found on the MSA web site, via the specific issue's Table of Contents (go to http://www.minsocam.org/MSA/AmMin/TOC/2017/Jul2017_data/Jul2017_data.html).



four framework oxygen and two H₂O molecules and after dehydration there are only four bonding interactions to the framework oxygen. This results in a significant under-bonding of the EFC (Fig. 3). Before and after dehydration, the ranges of interatomic distances between the EFC site and framework oxygen change slightly from 2.20(3)–3.02(3) to 2.24(5)–2.94(5) Å in the Li-NAT, and from 2.438(6)–2.772(8) to 2.461(8)–2.646(6) Å in the Ag-NAT (Supplemental¹ Table 2). Moreover, these EFCs have no bonding (O2-EFC-O2) across the channel. This means that the O2 site is no longer involved in bonding. The NAT chain can be rotated significantly and as a result the elliptic channel shape changes during dehydration. Compared to K-, Rb-, and Cs-NAT that are stable after dehydration and room temperature, the structures of Li- and Ag-NAT start to collapse and form a glass, which is most likely due to under-bonding of the EFC. Bond valence sum (BVS) values of monovalent EFCs are close to 1 in all hydrated models at ambient conditions. The bond valence sum (BVS) of the K⁺, Rb⁺, and Cs⁺ ions in dehydrated models are 0.74, 0.77, and 0.78, respectively, whereas Li⁺ and Ag⁺ cations are more under-bonded with BVS of less than 0.6 (Fig. 4). The deviation from the formal valence can be taken as a proxy for under-bonding of the EFC and explains why dehy-

▼ FIGURE 1. Changes of the synchrotron X-ray powder diffraction patterns of (a) Li-NAT, (b) Ag-NAT, and (c) Cs-NAT as a function of temperature; 300 K patterns in a and c were measured after exposing the samples to ambient conditions for a week. Asterisk marks in a indicate peaks from the impurity. (Color online.)



hydrated K-, Rb-, and Cs-NAT are more stable. In contrast, both Li^+ and Ag^+ ions are located in positions that are significantly more under-bonded. The location of an EFC that can bond to O2 sites might be an important factor that prohibits framework collapse and subsequent amorphization.

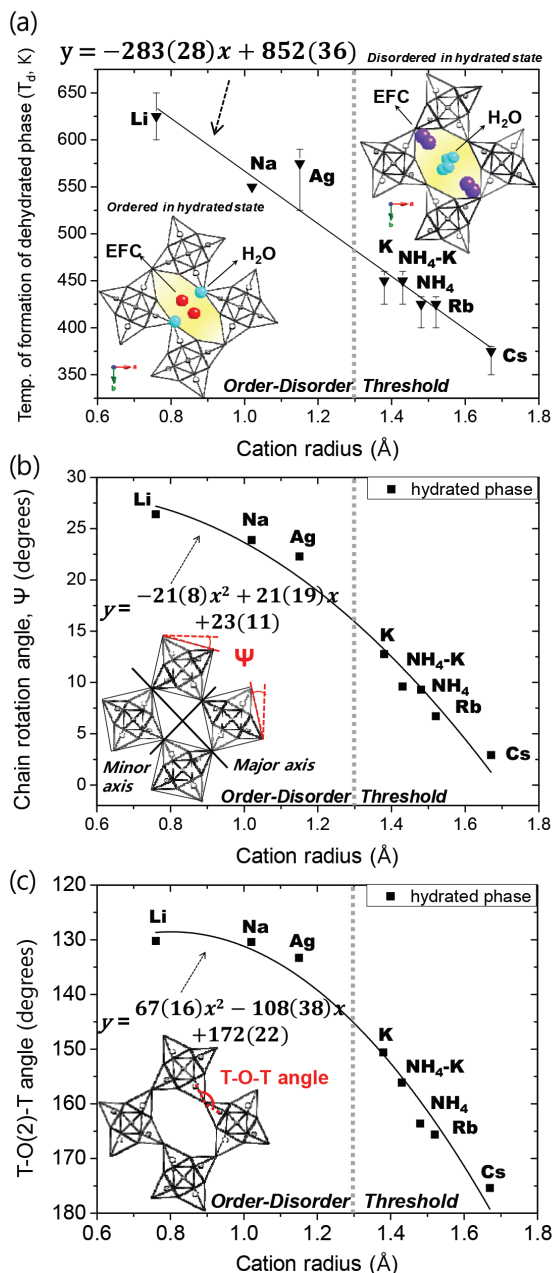


FIGURE 2. Dependency of the (a) onset of dehydration temperature of NAT phases (T_d), (b) chain rotation angle, and (c) T-O(2)-T angle as a function of extra-framework cation (EFC) size. Labels indicate the EFC of NAT. Dashed vertical line near 1.3 \AA represents possible threshold of order-disorder transition in the EFC and H_2O distribution in NAT channel (Lee et al. 2011b). Error values in **a** are estimated based on the calibration using NaCl standard. Estimated standard deviations (e.s.d. values) in **b** and **c** are smaller than the size of each symbol. (Color online.)

Our previous dehydration studies of NAT analogs with monovalent EFC established that the temperature of formation of dehydrated phase, T_d , decreases proportional with EFC size (Fig. 2a). Na-NAT starts to dehydrate at 550(20) K while Cs-NAT dehydrates at 375(25) K. Both Li- and Ag-NAT follow this trend. There are other trends observed in monovalent NAT analogs and their dehydrated phases: the unit-cell volumes of both hydrated and dehydrated forms have a linear relationship with EFC size (Supplemental¹ Fig. 2a).

The chain rotation angle of Cs-NAT [$\psi = 2.9(1)^\circ$] indicates the most circular channels while Li-NAT [$\psi = 26.4(2)^\circ$] has the most elliptical ones. After losing H_2O molecules during dehydration the channel contracts and stabilizes the structure. The chain rotation angles of the dehydrated phases are thus usually higher than those of hydrated phases. Values of ψ for the dehydrated phases between 625(25) and 675(25) K reveal an inversely linear trend with cation size (Supplemental¹ Fig. 2b). The angles of both hydrated Li-NAT and Ag-NAT are $26.4(2)^\circ$ and $22.3(2)^\circ$, respectively. The angles of their dehydrated phases become $-29.6(2)^\circ$ (Li-NAT) and $-23.4(2)^\circ$ (Ag-NAT), the minus sign indicating an inversion of the channel orientation in the a - b plane.

Only Li-NAT and Ag-NAT undergo reorientations of their channels through an intermediate circular channel at $\psi = 0^\circ$ during dehydration. Li-NAT has the most elliptical channel of all NAT analogs with monovalent EFC before and after dehydration. The shape of the channels can be described by a chain bridging angle, T(Si, Al)-O(2)-T (Fig. 2c). In hydrated NAT analogs, the T-O(2)-T angle exponentially increases as a function of EFC size. The angle is $130.2(4)^\circ$ in Li-NAT and increases to an almost linear T-O(2)-T configuration of $175.4(4)^\circ$ in Cs-NAT. In hydrated Ag-NAT the T-O(2)-T angle is $133.3(4)^\circ$ at room temperature. Although the data are somewhat scattered, T-O(2)-T angles in dehydrated phases also increase with EFC size. Decrease of the T-O(2)-T angles are comparatively small in Li-NAT [from $130.2(4)^\circ$ to $124(4)^\circ$] and Ag-NAT [from $133.3(4)^\circ$ to $127.1(3)^\circ$]. (See Supplemental¹ Fig. 2c.)

Thermal expansion coefficients of NAT analogs are shown in Figure 5. For both hydrated and dehydrated Li- and Ag-NAT, the magnitude of thermal expansion varies inversely with the size of the EFC (Fig. 5). The thermal expansion coefficients are positive in the hydrated state and negative after dehydration. This behavior is in contrast to what is observed in hydrated and dehydrated Na-NAT where negative and positive thermal expansion coefficient, respectively, are observed. These three NAT analogs are isostructural with EFC being located near the center of the channels and the H_2O molecules in closer proximity to the aluminosilicate framework.

The negative thermal expansion coefficients for the hydrated K-, Rb-, and Cs-NAT are linearly proportional to the EFC size while those of the dehydrated K-, Rb-, and Cs-NAT have positive values and do not vary linearly with the EFC size. These three NAT analogs are members of a second structural family where the disordered H_2O molecules are found near the center of the channels and the EFC in close proximity to the aluminosilicate framework.

Temperature-dependent changes of the unit-cell constants were modeled by whole profile fitting, and the values of the normalized volumes are shown in supporting Figure 1. While

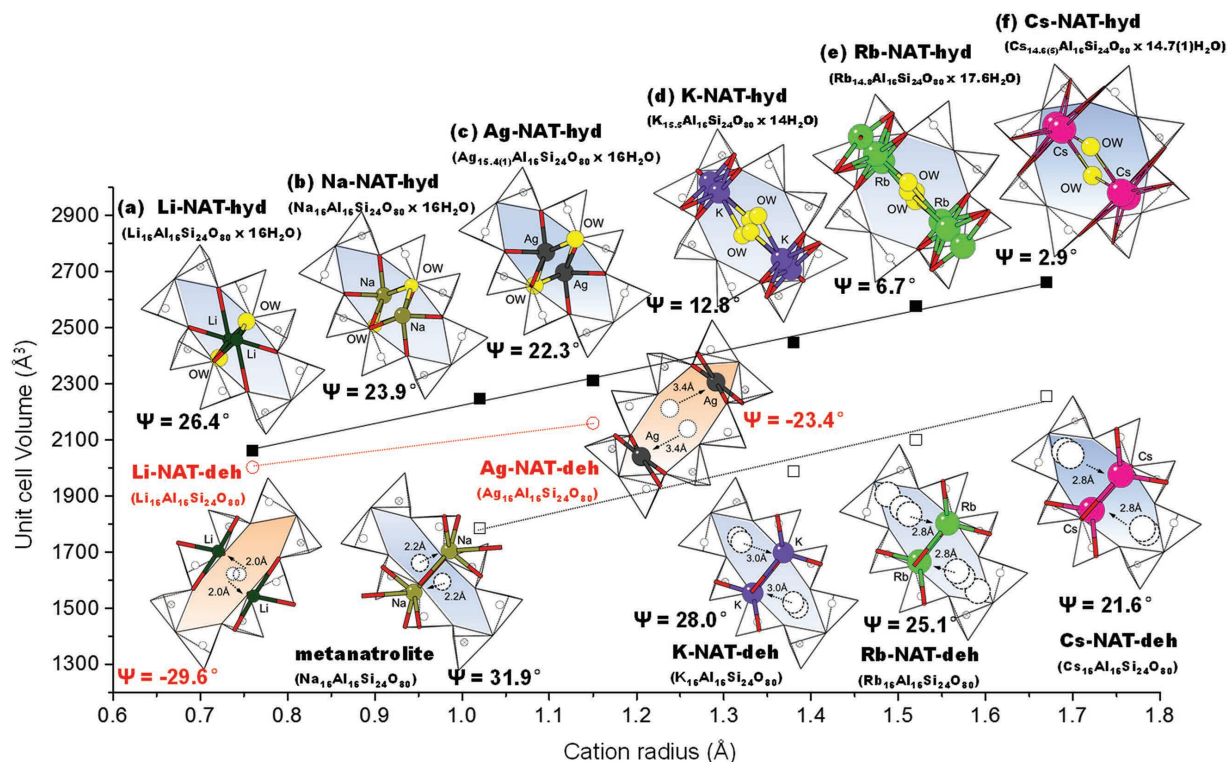


FIGURE 3. Structures of the hydrated and dehydrated phases of (a) Li-NAT, (b) Na-NAT, (c) Ag-NAT, (d) K-NAT, (e) Rb-NAT, and (f) Cs-NAT viewed along [001] (Baur and Joswig 1996; Lee et al. 2010, 2011c). Yellow circles show oxygen atoms of H₂O molecules. Dark green, dark yellow, black, violet, green, and purple circles represent the extra-framework cations, Li⁺, Na⁺, Ag⁺, K⁺, Rb⁺, and Cs⁺, respectively. (Color online.)

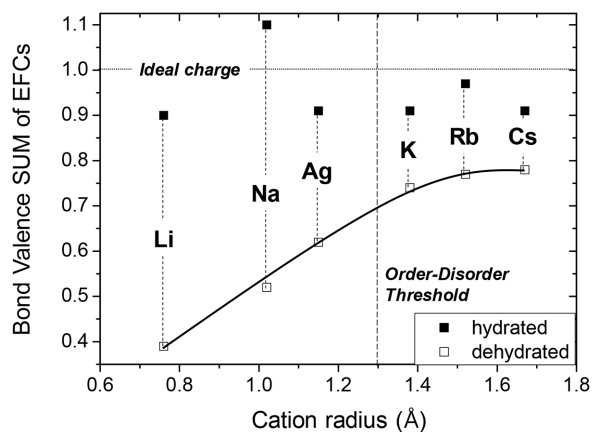


FIGURE 4. Bond Valence Sum (BVS) values of the EFCs depending on cation size. Labels indicate cation-substituted NAT. Dashed vertical line near 1.3 Å represents possible threshold of order-disorder transition in the EFC and H₂O distribution in NAT channel (Lee et al. 2011b). BVS values of Na⁺, K⁺, and Rb⁺ cations are from references (Baur and Joswig 1996; Lee et al. 2011c).

the unit-cell volume of Li-NAT shows two distinct linear expansion regions before and after 300 K (Supplemental¹ Fig. 1a), the unit-cell volumes of Ag- and Cs-NAT expand linearly over the temperature range (Supplemental¹ Figs. 1b and 1c). The hydrated

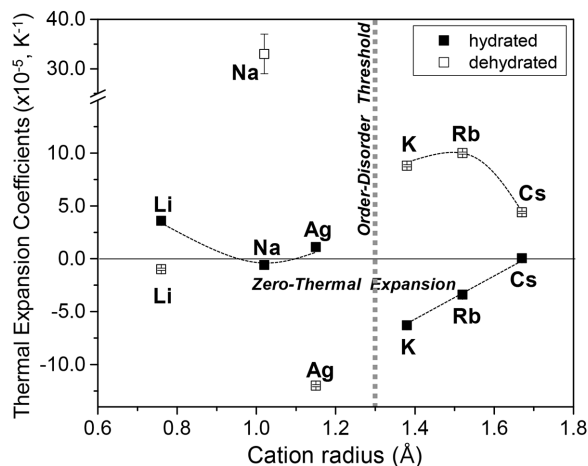


FIGURE 5. Thermal expansion coefficients of NAT analogs before T_d (hydrated) and after T_d (dehydrated). Dashed vertical line near 1.3 Å represents possible threshold of order-disorder transition in the EFC and H₂O distribution in NAT channel (Lee et al. 2011b).

NAT phases exhibit very low thermal expansion. Across 300 K, the thermal coefficient of Li-NAT increases from $1.3(1) \times 10^{-5} \text{ K}^{-1}$ (75–300 K) to $3.6(1) \times 10^{-5} \text{ K}^{-1}$ (300–450 K). Coefficients of Ag-NAT and Cs-NAT are $1.1(1) \times 10^{-5} \text{ K}^{-1}$ (75–475 K) and $3.0(1)$

$\times 10^{-6} \text{ K}^{-1}$ (75–350 K), respectively. Cs-NAT shows the lowest thermal expansion coefficient among all NAT analogs with $3.0(1) \times 10^{-6} \text{ K}^{-1}$ between 75 and 350 K. After dehydration, Li-, Ag-, and Cs-NAT contract without any indication of a phase transition. Up to 700 K the unit-cell volume of Cs-NAT expands at a rate of $4.4(1) \times 10^{-5} \text{ K}^{-1}$ (375–700 K). In contrast, Li- and Ag-NAT show “negative thermal expansion” (NTE) with $-1.0(1) \times 10^{-5} \text{ K}^{-1}$ between 625 and 725 K and $-1.2(1) \times 10^{-4} \text{ K}^{-1}$ between 575 and 625 K, respectively (Fig. 5).

In a previous dehydration study, amorphization was observed in NH_4 -NAT (Lee et al. 2011a). The recovered phase of fully NH_4 -exchanged NAT after dehydration is amorphous. Temperature-induced amorphization is observed after dehydration in both Li- and Ag-NAT whereas Cs-NAT remains crystalline after dehydration. The Bragg reflections of Li-NAT gradually decrease at higher temperatures. A recrystallization of the recovered phase at ambient conditions is not observed after a week. Diffraction peaks of Ag-NAT disappear abruptly within 50 K after dehydration. After exposure to ambient conditions for a week, dehydrated Ag-NAT remains in an amorphous state. Concomitant with the temperature-induced amorphization of the isostructural Li- and Ag-NAT one notices a significant underbonding of the EFC in the dehydrated phase as shown in Figure 3.

In contrast to Li- and Ag-NAT, the Na-NAT structure appears to be more stable during the dehydration and rehydration processes. According to Baur and Joswig (1996), heating the single-crystal Na-NAT to 548 K yields a dehydrated phase called metanatotrolite ($\text{Na}_{16}\text{Al}_{16}\text{Si}_{24}\text{O}_{80}$). The symmetry is reduced from *Fdd2* to *F112* concomitant with an abrupt volume contraction from 2250 to 1785 \AA^3 . Further heating to 773 K induces volume expansion of metanatotrolite and above 823 K metanatotrolite transforms to β -metanatotrolite (*F112*, $\text{Na}_{16}\text{Al}_{16}\text{Si}_{24}\text{O}_{80}$, $V = 2016 \text{ \AA}^3$), which coexists with an unknown impure phase. After thermal annealing for 50 h at 823 K, the β -metanatotrolite transforms into high-natrolite (*Fdd2*, $\text{Na}_{16}\text{Al}_{16}\text{Si}_{24}\text{O}_{80}$, 1960 \AA^3). Upon cooling the high natrolite to 293 K, post-natrolite (*Fdd2*, $\text{Na}_{16}\text{Al}_{16}\text{Si}_{24}\text{O}_{80} \cdot 16\text{H}_2\text{O}$, 2183 \AA^3) is formed by rehydration near 373 K. As the temperature increases to 548 K, the Na^+ cations migrate to the sides in the NAT channel where they occupy three statistically disordered positions. Above 823 K, the disordered distribution becomes enhanced and the Na^+ cation sites split further into four statistical positions both at the sides and the middle of the channel with 25% occupancy. These sites are all coordinated by five framework oxygen atoms where the Na^+ cation bridges O(2) atoms across the channel. On the contrary, in the dehydrated Li- and Ag-NAT, the coordination of EFC by framework oxygen atoms is four and does not bridge the O(2) atoms across the channel (Fig. 3). Overall, the dehydrated forms of Li- and Ag-NAT remain amorphous while the recovered Na-NAT and Cs-NAT are crystalline.

To further probe the bonding interaction of EFC and H_2O molecules in the channels of NAT analogs we measured the X-ray absorption spectra (XAS) at the oxygen *K*-edge (Fig. 6). In previous work the main- and post-edge XAS spectra of oxygen have been related to bonding interactions of the EFC and the aluminosilicate framework oxygen and the H_2O molecules in the NAT channel, respectively (Lee et al. 2013). As the cation radius and ionic potential varies the position of the main peak decreases and

increases, respectively. This reflects the increase of the basicity of the framework oxygen as the electronegativity increases from Cs to Li enhancing the negative charge on the framework O atoms. As noted by Vayssilov and Rösch the O1s binding energy shift is a measure of the basicity of oxygen in alkali-exchanged zeolites (Vayssilov and Rösch 1999). The post-edge feature characterizing the interaction between the H_2O molecules and the cations show a nice separation of NAT analogs with disordered H_2O molecules in the center of the channels and lower binding energies (K-, NH_4 -, Rb-, and Cs-NAT) and those in close proximity to the aluminosilicate framework (Li- and Ag-NAT) that are stronger bonded. In K-, NH_4 -, Rb-, and Cs-NAT a linear relationship of the interaction energy and both EFC radius and ionic potential is observed. In Li- and Ag-NAT the H_2O molecule has a stronger interaction with the aluminosilicate framework [540.6(1) and 540.8(1) eV, respectively] than K-NAT, which has the weakest bonding energy with 539.8(1) eV. This is corroborated by the DFT studies of Kremleva et al. (2013).

In this study, we found that the dehydrated phases of Li-, Ag-, and Cs-NAT form at 625(25), 575(50), and 375(25) K, respectively. The dehydration temperatures show an inverse relationship with the EFC size. Thermal expansion varies with the size of the EFC, EFC- H_2O topologies and H_2O -O_f. Changing the orientation of the channel ellipticity in Li- and Ag-NAT has been correlated to the migration of the EFCs from the middle to the wall of the pores during dehydration. Structural collapse and amorphization has been induced by changes in the coordination between EFC and framework after dehydration.

IMPLICATIONS

Since its first discovery by Klaproth in 1803 and structural report by Pauling in 1930, NAT has been studied by numerous researchers as a model zeolite with well-defined composition and structure. The limited cation-exchange property of NAT, however, hindered comparative understanding of its crystal chemistry as a function of extra-framework cations (EFCs), temperature, degree of hydration, and pressure. In 1986, Yamazaki et al. reported that the cation exchange rate of NAT can be increased up to 91.94% using KCl solution at ambient condition for 62 days. They also showed that the endotherm peak of NAT shifts from ca. 300 to ca. 150 °C after exchanging Na^+ by K^+ , which indicates that dehydration temperature decreases by means of K^+ exchange. The structural model of K-NAT has been proposed to be different from that of the original Na-NAT.

To understand the structural difference of the two compounds, we have previously used combined X-ray absorption spectroscopy (XAS) and X-ray powder diffraction (XRD) on a series of partially and fully K-NAT (Lee et al. 2013), which revealed the disordered distribution of the cation- H_2O assembly in the channels of the K-form compared to the ordered one in the original Na-form. Further XAS results showed that the bonding energy between H_2O and framework oxygen atoms has decreased in the K-form due to the migration of H_2O to the middle of the channel. These results indicate that K-form would have more capability of ion-exchange than the original NAT, which led to the successful generation of a series of different cation forms of NAT analogs and their comparative structural and thermochemical understanding at ambient conditions and high pressure (Lee et al.

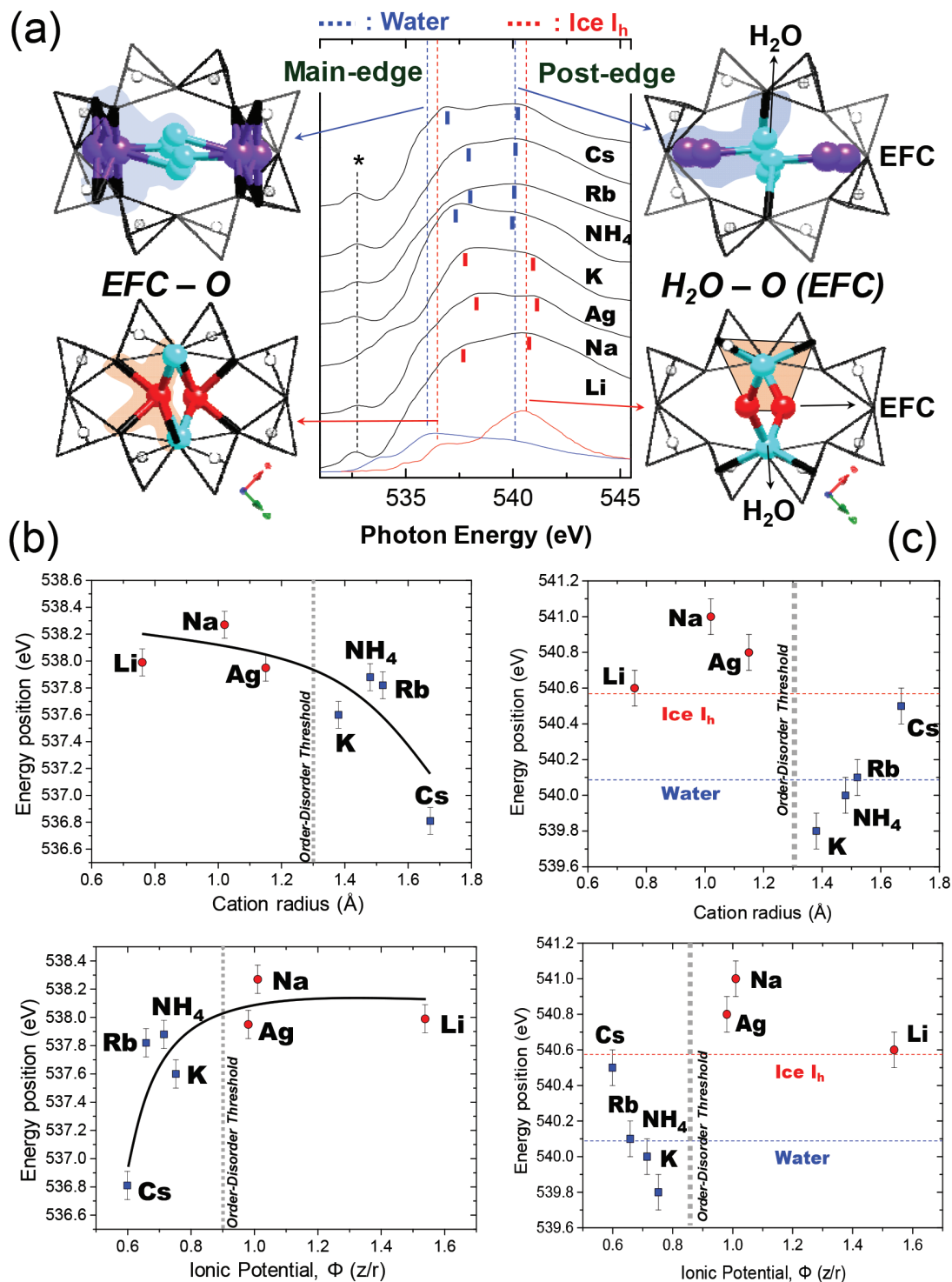


FIGURE 6. (a) X-ray absorption spectra of NAT analogs at the oxygen *K*-edge. Red and blue solid lines on the bottom are reference spectra of the bulk Ice I_h and bulk water, respectively (Wernet et al. 2004). Asterisk marks indicate signals from the carbon tape used as a sample holder. (b) Plot of the oxygen bonding energy at the main-edge of NAT analogs as a function of cation size or ionic potential. Labels indicate each cation-substituted NAT. (c) Plot of the oxygen bonding energy at the post-edge of NAT analogs as a function of cation size or ionic potential. Labels indicate the EFC of the NAT. (Color online.)

2010, 2011b; Seoung et al. 2013, 2015; Wu et al. 2013). Following our previous high-temperature investigation of K-, Rb-, and Cs-NAT (Lee et al. 2011c), this paper completes the comparative structural understanding of monovalent cation forms of NAT.

We suggest that different cation forms of NAT might exist in nature under suitable environmental conditions but could be difficult to find as the structural changes induced by cation exchange exert significant volume changes by ca. 10% in the case of K-exchange and up to 19% in the case of Cs-exchange when compared to the unit-cell volume of the original NAT. Previous thermodynamic data determined by high-temperature oxide melt solution calorimetry established that the formation enthalpy is more exothermic as the ionic potential decreases in cation exchanged NAT (Wu et al. 2013). Zeolites containing EFCs with smaller ionic potential are thus expected to be more stable. The type of EFC is more important for the structural stability than the degree of hydration. A similar trend is shown for the substitution energy as a function of the ionic potential with different EFCs. The structures of all monovalent cation forms of NAT have now been determined at high pressures and high temperatures, i.e., EFC-dependent pressure-induced hydration in the presence of H₂O and systematic variations of the dehydration temperatures and thermal expansion with different EFCs and ionic potential were established.

ACKNOWLEDGMENTS

This work was supported by the Global Research Laboratory (NRF-2009-00408) and National Research Laboratory (NRF-2015R1A2A1A01007227) Programs of the Korean Ministry of Science ICT and Planning (MSIP). We also thank the support of the NRF grants 2016K1A4A3914691 and 2016K1A3A7A09005244. In situ XRD experiment was performed at PAL, supported in part by the MEST and POSTECH, and at NSLS. XAS experiment was carried out at the SSRL, a Directorate of SLAC and an Office of Science User Facility operated by Stanford University for the U.S. Department of Energy Office of Science.

REFERENCES CITED

- Baur, W.H., and Joswig, W. (1996) The phases of natrolite occurring during dehydration and rehydration studied by single-crystal X-ray diffraction methods between room temperature and 923K. *Neues Jahrbuch für Mineralogie*, 171–187.
- Dollase, W.A. (1986) Correction of intensities for preferred orientation in powder diffractometry: Application of the March Model. *Journal of Applied Crystallography*, 19, 267–272.
- Fang, J.H. (1963) Cell dimensions of dehydrated natrolite. *American Mineralogist*, 48, 414–417.
- Hwang, G.C., Shin, T.J., Blom, D.A., Vogt, T., and Lee, Y. (2015) Pressure-induced amorphization of small pore zeolites—the role of cation-H₂O topology and anti-glass formation. *Scientific Reports*, 5, 15056.
- Klaproth, M.H. (1803) *Gesellschaft Naturforschende Freunde zu Berlin, Neue Schriften*, 4, 243–248.
- Kremleva, A., Vogt, T., and Röscher, N. (2013) Monovalent cation-exchanged natrolites and their behavior under pressure. A computational study. *Journal of Physical Chemistry C*, 117, 19,020–19,030.
- Larson, A., and von Dreele, R.B. (1986) General Structure Analysis System (GSAS). Los Alamos National Laboratory, New Mexico, Report LAUR, 86-748.
- Lee, Y., Lee, Y., and Seoung, D. (2010) Natrolite may not be a “soda-stone” anymore: Structural study of fully K-, Rb-, and Cs-exchanged natrolite. *American Mineralogist*, 95, 1636–1641.
- Lee, Y., Seoung, D., Jang, Y.N., Bai, J., and Lee, Y. (2011a) Structural studies of NH₄-exchanged natrolites at ambient conditions and high temperature. *American Mineralogist*, 96, 1308–1315.
- Lee, Y., Seoung, D., and Lee, Y. (2011b) Natrolite is not a “soda-stone” anymore: Structural study of alkali (Li⁺), alkaline-earth (Ca²⁺, Sr²⁺, Ba²⁺) and heavy metal (Cd²⁺, Pb²⁺, Ag⁺) cation-exchanged natrolites. *American Mineralogist*, 96, 1718–1724.
- Lee, Y., Seoung, D., Liu, D., Park, M.B., Hong, S.B., Chen, H., Bai, J., Kao, C.-C., Vogt, T., and Lee, Y. (2011c) In-situ dehydration studies of fully K-, Rb-, and Cs-exchanged natrolites. *American Mineralogist*, 96, 393–401.
- Lee, Y., Lee, J.-S., Kao, C.-C., Yoon, J.-H., Vogt, T., and Lee, Y. (2013) Role of cation–water disorder during cation exchange in small-pore zeolite sodium natrolite. *The Journal of Physical Chemistry C*, 117, 16119–16126.
- Pauling, L. (1930) The structure of some sodium and calcium aluminosilicates. *Proceedings of the National Academy of Sciences*, 16, 453–459.
- Reeuwijk, V. (1972) High-temperature phases of zeolites of the natrolite group. *American Mineralogist*, 57, 499–510.
- Rietveld, H.M. (1969) A profile refinement method for nuclear and magnetic structures. *Journal of Applied Crystallography*, 2, 65–71.
- Rinne, F. (1890) Über die umänderungen welche die zeolithe durch erwärmen bei und nach dem trübwerden erfahren. *Sitzungsberichte der Preussischen Akademie der Wissenschaften, Physikalisch-Mathematische Klasse*, 46, 1163–1207.
- Seoung, D., Lee, Y., Kao, C.C., Vogt, T., and Lee, Y. (2013) Super-hydrated zeolites: Pressure-induced hydration in natrolites. *Chemistry—A European Journal*, 19, 10,876–10,883.
- Seoung, D., Lee, Y., Kao, C.C., Vogt, T., and Lee, Y. (2015) Two-step pressure-induced superhydration in small pore natrolite with divalent extra-framework cations. *Chemistry of Materials*, 27, 3874–3880.
- Stahl, K., and Hanson, J. (1994) Real-time X-ray synchrotron powder diffraction studies of the dehydration processes in scolecite and mesolite. *Journal of Applied Crystallography*, 27, 543–550.
- Thompson, P., Cox, D.E., and Hastings, J.B. (1987) Rietveld refinement of Debye-Scherrer synchrotron X-ray data from Al₂O₃. *Journal of Applied Crystallography*, 20, 79–83.
- Toby, B.H. (2001) EXPGUI, a graphical user interface for GSAS. *Journal of Applied Crystallography*, 34, 210–213.
- Vayssilov, G.N., and Röscher, N. (1999) Density functional studies of alkali-exchanged zeolites: Basicity and core-level shifts of framework oxygen atoms. *Journal of Catalysis*, 186, 423–432.
- Wang, H.-W., and Bish, D.L. (2008) A *P*_{H₂O}-dependent structural phase transition in the zeolite natrolite. *American Mineralogist*, 93, 1191–1194.
- Wernet, P., Nordlund, D., Bergmann, U., Cavalleri, M., Odelius, N., Ogasawara, H., Näslund, L.Å., Hirsch, T.K., Ojamäe, L., Glatzel, P., Pettersson, L.G.M., and Nilsson, A. (2004) The structure of the first coordination shell in liquid water. *Science*, 304, 995–999.
- Wu, L., Navrotsky, A., Lee, Y., and Lee, Y. (2013) Thermodynamic study of alkali and alkaline-earth cation-exchanged natrolites. *Microporous and Mesoporous Materials*, 167, 221–227.
- Yamazaki, A., Otsuka, R., and Nishido, H. (1986) The thermal behavior of K-exchanged forms of natrolite. *Thermochimica Acta*, 109, 237–242.

MANUSCRIPT RECEIVED JUNE 27, 2016

MANUSCRIPT ACCEPTED FEBRUARY 26, 2017

MANUSCRIPT HANDLED BY G. DIEGO GATTA